

Vortex clusters and their active control in a cold Rydberg atomic system with $\mathcal{PT}$-symmetric Bessel potential

Zhuo Fan(范灼), Yi Shi(石逸), Hang Wang(王航), Yuan Zhao(赵元), Wei Peng(彭微), and Siliu Xu(徐四六)

Citation: Chin. Phys. B, 2024, 33 (**12**): 120306. DOI: 10.1088/1674-1056/ad8073
Journal homepage: http://cpb.iphy.ac.cn; http://iopscience.iop.org/cpb

What follows is a list of articles you may be interested in

Bessel vortices in spin-1 Bose-Einstein condensates with Zeeman splitting and spin-orbit coupling

Huan-Bo Luo(罗焕波), Xin-Feng Zhang(张鑫锋), Runhua Li(李润华), Yongyao Li(黎永耀), and Bin Liu(刘彬)
Chin. Phys. B, 2024, 33 (**10**): 100304. DOI: 10.1088/1674-1056/ad6424

Coulomb-assisted nonlocal electron transport between two pairs of Majorana bound states in a superconducting island

Hao-Di Wang(王浩迪), Jun-Tong Ren(任俊潼), Hai-Feng Lü(吕海峰), and Sha-Sha Ke(柯莎莎)
Chin. Phys. B, 2024, 33 (**5**): 050310. DOI: 10.1088/1674-1056/ad2a68

Coherence of nonlinear Bloch dynamics of Bose—Einstein condensates in deep optical lattices

Ai-Xia Zhang(张爱霞), Wei Zhang(张薇), Jie Wang(王杰), Xiao-Wen Hu(胡潇文), Lai-Lai Mi(米来来), and Ju-Kui Xue(薛具奎)
Chin. Phys. B, 2024, 33 (**4**): 040305. DOI: 10.1088/1674-1056/ad1b46

Dynamical nonlinear excitations induced by interaction quench in a two-dimensional box-trapped Bose-Einstein condensate

Zhen-Xia Niu(牛真霞) and Chao Gao(高超)
Chin. Phys. B, 2024, 33 (**2**): 020314. DOI: 10.1088/1674-1056/ad1179

Rydberg quantum controlled-phase gate with one control and multiple target qubits

S L Su(苏石磊)
Chin. Phys. B, 2018, 27 (**11**): 110304. DOI: 10.1088/1674-1056/27/11/110304

Vortex clusters and their active control in a cold Rydberg atomic system with $\mathcal{PT}$-symmetric Bessel potential

Zhuo Fan(范灼)[1,2,†], Yi Shi(石逸)[1,3,†], Hang Wang(王航)[1,3], Yuan Zhao(赵元)[1,2], Wei Peng(彭微)[1,2,‡], and Siliu Xu(徐四六)[1,2,§]

[1] *Key Laboratory of Optoelectronic Sensing and Intelligent Control, Hubei University of Science and Technology, Xianning* 437100, *China*
[2] *School of Biomedical Engineering and Imaging, Xianning Medical College, Hubei University of Science and Technology, Xianning* 437100, *China*
[3] *School of Electronic and Information Engineering, Hubei University of Science and Technology, Xianning* 437100, *China*

(Received 29 July 2024; revised manuscript received 16 September 2024; accepted manuscript online 27 September 2024)

We propose an approach for generating robust two-dimensional (2D) vortex clusters (VCs) in a Rydberg atomic system by utilizing parity-time ($\mathcal{PT}$) symmetric optical Bessel potential. We show that the system supports novel multi-core VCs with four and eight cores, corresponding to topological charges 2 and 4, respectively. The stability of these VCs can be dynamically adjusted through the manipulation of the gain-loss component, Kerr nonlinearities, and the degree of nonlocality inherent in the Rydberg atoms. These VCs are confined within the first lattice well of the Bessel potential, and both the power and width of lights undergo a quasi-periodic breathing phenomenon, which is attributed to the power exchange between the light fields and Bessel potential. Both self-attractive and self-repulsive Kerr interactions can sustain robust VCs within this system. The insights presented here not only facilitate the creation and manipulation of 2D VCs through $\mathcal{PT}$-symmetric potentials but also pave the way for potential applications in optical information processing and transmission.

Keywords: vortex clusters, $\mathcal{PT}$ symmetry, Bessel potential, Rydberg–Rydberg interaction

PACS: 03.75.Lm, 11.30.Er, 32.80.Ee **DOI:** 10.1088/1674-1056/ad8073

1. Introduction

Over the past few decades, nonlinear optical beam control has garnered significant research attention owing to its key role in elucidating the fundamental physics of nonlinear optical processes and exploring practical applications of diverse nonlinear optical techniques.[1,2] Among the various methodologies proposed for manipulating optical solitons, a noteworthy approach is utilizing spatial variations in optical medium properties induced by modulated control laser fields, such as refractive index, gain and loss. According to these proposals, numerous novel optical solitons, absent in uniform nonlinear media, have been uncovered.[3,4] Theoretical predictions,[5–8] and experimental observations[9,10] have corroborated the existence of fundamental, multipole, and vortex solitons by modulating refractive index.

To meet the requirement for intense laser fields or extended propagation distances when realizing optical solitons, the concept of resonant atomic gas working under electromagnetically induced transparency (EIT) conditions has been proposed.[11–13] Through the quantum interference effect induced by a control laser field, the absorption of a probe laser field tuned to a strong one-photon resonance is significantly suppressed, rendering the optical medium transparent. Consequently, the Kerr nonlinearity of the system undergoes substantial enhancement. Unlike conventional cold atom EIT systems, Rydberg electromagnetically induced transparency (Rydberg-EIT) systems exhibit the capability to manipulate light fields through significant non-local nonlinearities.

The Rydberg cold atom system is attracting significant attention owing to its advanges, such as large principal quantum number and long lifetime. It offers immense potential for applications in diverse fields such as quantum information, precision spectroscopy, precision measurement, and quantum multi-state manipulation.[14–18] The robust atomic interactions can be translated into the photonic domain through the coupling between Rydberg atomic ensembles and photons, providing a practical framework for investigating quantum nonlinear optics.[19] This enables the realization of nonlocal nonlinear manipulation of light fields.[20–22] Based on these findings, Rydberg-EIT provides an excellent platform for spatial soliton propagation, facilitating the discovery of a series of high-dimensional spatial solitons.[23–25]

An additional advantage of Rydberg-EIT atomic media is the high proficiency in designing optical potentials by modulating the control and auxiliary light field.[26,27] Due to the intricate nature of optical potentials in Rydberg-EIT media, they can be precisely designed in both their real and imaginary components, corresponding to the refractive index and absorption (or gain) of the system, respectively. Taking these factors into account, recent studies have proposed and successfully implemented the construction of complex optical potentials that exhibit parity-time ($\mathcal{PT}$) symmetry in atomic gases.[28–32]

[†]These authors contributed equally to this work.
[‡]Corresponding author. E-mail: vivipw7958@163.com
[§]Corresponding author. E-mail: xusiliu1968@163.com

© 2024 Chinese Physical Society and IOP Publishing Ltd

The system characterized by a $\mathcal{PT}$-symmetric Hamiltonian can support entirely real eigenvalues and facilitate a transition from a purely real spectrum to a complex one.[33] In optics, the breaking of $\mathcal{PT}$-symmetry manifests as a qualitative modulation in light propagation, which has numerous significant applications.[34,35] Predictions of optical solitons have been made in nonlinear optical media with diverse $\mathcal{PT}$-symmetric potentials.[36–38] Moreover, the existence of fundamental, dipole, and multipeak solitons has been observed in nonlinear media endowed with $\mathcal{PT}$-symmetric Bessel potentials.[39–42] However, the investigation of 2D vortex clusters (VCs) that propagate stably in a cold Rydberg atomic system with $\mathcal{PT}$-symmetric optical Bessel potential remains unexplored. A practical system to realize the $\mathcal{PT}$-symmetric Bessel potential and VCs control is also needed. In this work we propose a scheme to realize an optical Bessel potential with $\mathcal{PT}$-symmetry and explore the possibility of the existence, robust propagation, and active manipulation of VCs in such a $\mathcal{PT}$-symmetric system.

2. Model

In this study, we investigate a four-level inverted-Y atomic system dressed with Rydberg states, as depicted in Fig. 1(a). Each atom comprises four energy levels, denoted as $|1\rangle$, $|2\rangle$, $|3\rangle$, and $|4\rangle$. A weak probe beam (with frequency $\omega_{\rm p}$ and half-Rabi frequency $\Omega_{\rm p}$) couples the energy levels $|1\rangle$, and $|3\rangle$, while a control beam (with frequency $\omega_{\rm c}$ and half-Rabi frequency $\Omega_{\rm c}$) couples the energy levels $|2\rangle$, and $|3\rangle$. Additionally, an auxiliary beam (with frequency $\omega_{\rm a}$ and half-Rabi frequency $\Omega_{\rm a}$) interacts with the Rydberg state $|4\rangle$ from level $|3\rangle$, thereby establishing Rydberg-EIT, as shown in Fig. 1(b). Here, Γ_{mn} represents the spontaneous emission rate between energy levels $|m\rangle$ and $|n\rangle$. $\Delta_3 = \omega_{\rm p} - (\omega_3 - \omega_1)$ signifies the single-photon detuning, while $\Delta_2 = \omega_{\rm p} - \omega_{\rm c} - (\omega_2 - \omega_1)$ and $\Delta_4 = \omega_{\rm p} + \omega_{\rm a} - (\omega_4 - \omega_1)$ correspond to the two-photon detunings, where ω_m is the frequency associated with the atomic energy level $|m\rangle$. The proposed scheme employs a coupling pump Γ_{21} to provide gain for the transition from energy level $|1\rangle$ to $|2\rangle$ in the system.

The dynamics of the system is described by the Hamiltonian $\hat{H}_{\rm H}(t) = N_{\rm a}\int_{-\infty}^{+\infty} {\rm d}^2\boldsymbol{r}\hat{H}_{\rm H}(\boldsymbol{r},t)$, where $N_{\rm a}$ is atomic density and $\boldsymbol{r} = (x,y)$ is the position vector of Rydberg atoms. Under electric-dipole and rotating-wave approximations, the Hamiltonian density in the interaction picture is

$$\begin{aligned}\hat{H}_{\rm H}(\boldsymbol{r},t) =& \sum_{m=1}^{4}\hbar\Delta_m\hat{S}_{mm}(\boldsymbol{r},t) - \hbar\big[\Omega_{\rm p}\hat{S}_{13}(\boldsymbol{r},t) + \Omega_{\rm a}\hat{S}_{34}(\boldsymbol{r},t)\\ &+\Omega_{\rm c}\hat{S}_{23}(\boldsymbol{r},t) + {\rm H.c.}\big]\\ &+N_{\rm a}\int {\rm d}^3\boldsymbol{r}'\hat{S}_{44}(\boldsymbol{r}',t)\hbar V(\boldsymbol{r}'-\boldsymbol{r})\hat{S}_{44}(\boldsymbol{r},t), \end{aligned}\tag{1}$$

where H.c. is Hermitian conjugate, $\hat{S}_{mn} = |n\rangle\langle m|\exp{\rm i}[(k_n - k_m)\cdot r - (\omega_n - \omega_m + \Delta_n - \Delta_m)t]$ is the transition operator related to states $|n\rangle$ and $|m\rangle$. $\Omega_{\rm p} = \left(\boldsymbol{e}_{\rm p}\cdot\boldsymbol{P}_{31}\right)\varepsilon_{\rm p}/\hbar$, $\Omega_{\rm c} = \left(\boldsymbol{e}_{\rm c}\cdot\boldsymbol{P}_{32}\right)\varepsilon_{\rm c}/\hbar$, and $\Omega_{\rm a} = \left(\boldsymbol{e}_{\rm a}\cdot\boldsymbol{P}_{43}\right)\varepsilon_{\rm a}/\hbar$ are the half Rabi frequencies of the probe, control, and auxiliary fields, with $\boldsymbol{P}_{mn}$ being the electric dipole matrix elements associated with the transition $|m\rangle \to |n\rangle$, and $\varepsilon_{\rm p/c/a}$ are dielectric constants of probe/control/auxiliary fields in the media. The interaction between different Rydberg atoms has the form of van der Waals potential $V_{\rm vdw} = \hbar V(\boldsymbol{r}'-\boldsymbol{r})$, where $V(\boldsymbol{r}'-\boldsymbol{r}) = C_6/\left[R_{\rm b}^6 + |\boldsymbol{r}'-\boldsymbol{r}|^6\right]$, C_6 is the dispersion parameter, $\boldsymbol{r}$ and $\boldsymbol{r}'$ are vector positions of two Rydberg atoms, $R_{\rm b}$ is the Rydberg blockade radius which can be obtained as $R_{\rm b} = \left[|C_6\Delta_3|/|\Omega_{\rm c}|^2\right]^{1/6}$.[24,25] The scheme of Rydberg atom and the corresponding energy level are shown in Figs. 1(a) and 1(b), respectively.

The dynamics of the motion of Rydberg atoms is governed by the optical Bloch equation[42] $\partial\hat{\rho}/\partial t = -({\rm i}/\hbar)[\hat{H}_{\rm H},\hat{\rho}] - \Gamma[\hat{\rho}]$, where ρ is the density matrix with elements are defined as $\rho_{mn} \equiv \langle\hat{S}_{mn}\rangle\,(m,n = 1\text{–}4)$, and Γ is relaxation matrix associated with the spontaneous emission rate. Under the slowly-varying amplitude approximation, the wave equation of the probe field has the form[25]

$${\rm i}\left(\frac{\partial}{\partial z} + \frac{1}{c}\frac{\partial}{\partial t}\right)\Omega_{\rm p} + \frac{1}{2k_{\rm p}}\left(\frac{\partial^2}{\partial x^2} + \frac{\partial^2}{\partial y^2}\right)\Omega_{\rm p} + \frac{k_{\rm p}}{2}\chi\Omega_{\rm p} = 0,\tag{2}$$

where $k_{\rm p} = \omega_{\rm p}/c$ is the wave number of probe field with c being the speed of light, $\chi = \boldsymbol{e}_{\rm p}\cdot\boldsymbol{P}_{13}^2\rho_{31}/(\varepsilon_0\hbar\Omega_{\rm p})$ is the susceptibility of probe field, ρ_{31} is the density element that can be obtained by the optical Bloch equations.

Supposing the probe field can be taken as a stationary nonlinear optical beam, the time-derivative terms in Eq. (2) can be neglected, i.e., $\partial/\partial t = 0$. By introducing rescaled coordinates, equation (2) can be expressed as the following nondimensional form[18,22,25]

$$\begin{aligned}&{\rm i}\frac{\partial\psi}{\partial\zeta} + \frac{1}{2}\nabla^2\psi + \gamma|\psi|^2\psi + V(\xi,\eta)\psi\\ &+\sigma\int {\rm d}^2\boldsymbol{r}'\frac{1}{(R_{\rm b}/r_0)^6 - |\boldsymbol{r}'-\boldsymbol{r}|^6}|\psi|^2\psi = 0,\end{aligned}\tag{3}$$

where the Laplace operator $\nabla^2 = \partial^2/\partial\xi^2 + \partial^2/\partial\eta^2$, $\psi = \Omega_{\rm p}/U_0$ with U_0 being the typical Rabi frequency. The longitudinal and the transverse coordinates are rescaled as $\zeta = z/L_{\rm diff}$ and $\boldsymbol{r} = (\xi,\eta) = (x,y)/r_0$, where $L_{\rm diff} = k_{\rm p}r_0^2$ and r_0 are diffraction length and beam width of probe field, respectively. γ and σ are the nondimensional coefficients of local and nonlocal nonlinearity, respectively.

The $V(\xi,\eta)$ is the external potential. In this work, in order to stabilize the probe field, the potential is taken as the Bessel form

$$V_{\rm Bessel}(\xi,\eta) = V_0 + V_1{\rm J}_0(\rho) + {\rm i}V_2{\rm J}_1(\rho)\sin(\theta),\tag{4}$$

where V_0 is a constant, V_1 and V_2 are the strength of the real and imaginary parts of Bessel potential with $V_1, V_2 \ll V_0$. ${\rm J}_i$ $(i = 0,1)$ is the i-th order Bessel function, and $\rho = \sqrt{\xi^2+\eta^2}$ and $\theta = \arcsin(\eta/\rho)$ are the radial and angular coordinates,

respectively. It is noted that the advantages of introduction of Bessel potential here is that the Bessel potential is much easier to capture light by the multi-potential wells. And the modulation strategy for topological structures of VCs is more richer. Figures 1(c) and 1(d) show distributions of the real and imaginary part of Bessel potential in the (ξ,η) plane. We see that the imaginary part of the potential $V_{\rm Bessel}(\xi,\eta)$ is an even function in the ξ direction and an odd function in the η direction, satisfying the $\mathcal{PT}$ symmetry condition, i.e., $V_{\rm Bessel}(\xi,\eta)^* = V_{\rm Bessel}(-\xi,-\eta)^*$, as shown in Fig. 1(e). Since the present system is highly configurable and manipulable, it is possible to create optical potentials with specific space distributions by modulating the control and auxiliary light fields in space.[42] To obtain stable solutions, the eigenvalues of wavefunctions should be all real, corresponding to $\mathcal{PT}$ symmetry. By tuning parameters V_1 and V_2, the $\mathcal{PT}$ symmetry-broken zones are depicted in Fig. 1(f).

The $\mathcal{PT}$ symmetric Bessel potential (4) can be obtained by using spatially modulated control and auxiliary fields with the following expression:[42]

$$\frac{\Omega_{\rm c}(\xi,\eta)}{\Omega_{\rm c0}} \approx 1+10^{-2}\times[0.62V_1{\rm J}_0(r)+1.98V_2{\rm J}_1(r)\sin(\theta)],$$
$$\frac{\Omega_{\rm a}(x,y)}{\Omega_{\rm a0}} \approx 1+10^{-2}\times[0.80V_1{\rm J}_0(r)+3.35V_2{\rm J}_1(r)\sin(\theta)], \quad (5)$$

where the initial half-Rabi frequency of control and auxiliary light field are $\Omega_{\rm c0}=\Omega_{\rm c}$ and $\Omega_{\rm a0}=\Omega_{\rm a}$, respectively.

For experimental consideration, the states of ^{87}Rb atoms can be taken as $|1\rangle = |5{\rm S}_{1/2},F=1\rangle$, $|2\rangle = |5{\rm S}_{1/2},F=2\rangle$, $|3\rangle = |5{\rm P}_{3/2}\rangle$, and $|4\rangle = |n{\rm S}_{1/2}\rangle$. Taken the principal quantum number $n=60$, we get $C_6 = 2\pi\times 140$ GHz$\cdot\mu$m^6.[42,43] The other system parameters are $U_0 = 150$ MHz, $r_0 = 10$ μm, $\Gamma_{21} = 2\pi\times 0.1$ MHz, $\Gamma_3 = \Gamma_{13}+\Gamma_{23} = 2\pi\times 16$ MHz, $\Gamma_4 = \Gamma_{34} = 2\pi\times 16.7$ kHz, $\Delta_2 = 1.67$ MHz, $\Delta_3 = 66.7$ MHz, $\Delta_4 = 13.6$ MHz, $\Omega_{\rm c} = 30$ MHz, and $\Omega_{\rm a} = 45$ MHz.[25] Suppose the light (with wavelength $\lambda = 760$ nm) propagates in the media (with refractive index ≈ 1.45), thus the diffraction length $L_{\rm diff} = 1.2$ mm, and $R_{\rm b} = 6.34$ μm. The unit of the scaled propagation distance and time are 1.2 mm and 10 μs, corresponding to $\zeta = 1$ and ξ or $\eta = 1$, respectively.

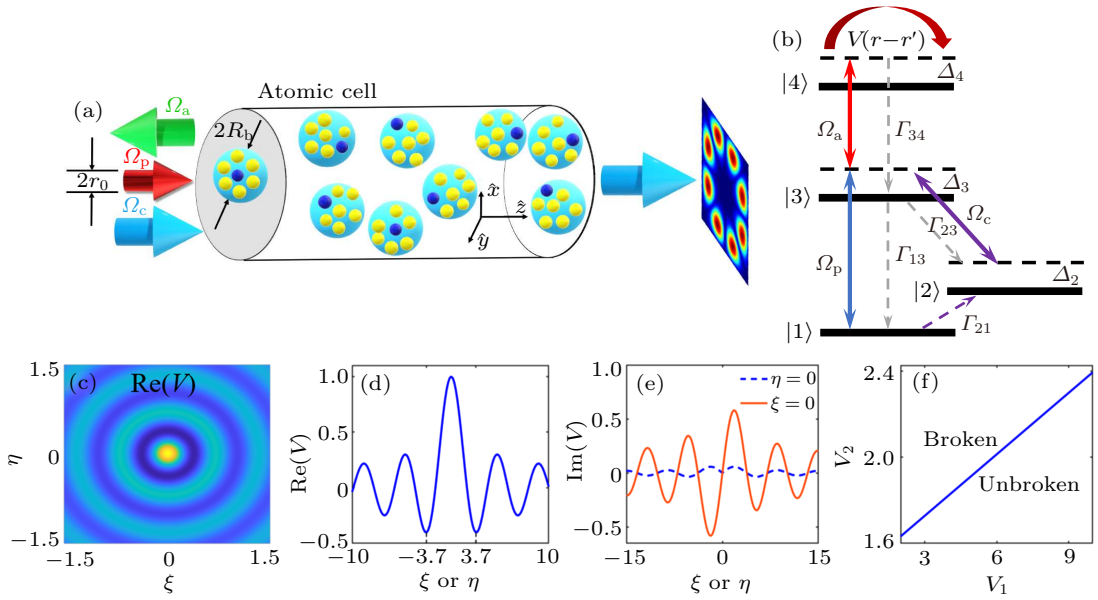


Fig. 1. Scheme of Rydberg-dressed $\mathcal{PT}$-symmetric Bessel potential system: (a) setup of cold Rydberg atomic system, (b) energy level structure, (c), (d) real part of Bessel potential in the (ξ,η) plane. The first lattice well of the Bessel potential is located at $\xi=\pm 3.7$ in the η direction. (e) Imaginary parts ${\rm Im}(V)$ in ξ or η direction. The solid and dashed lines, respectively, represent the Bessel potential distribution in the cross section with $\xi=0$ and $\eta=0$. (f) $\mathcal{PT}$-symmetry and $\mathcal{PT}$-symmetry broken zone in the (V_1,V_2) plane. The parameters for panels (c), (d), and (e) are $(V_0,V_1,V_2)=(0,1,1)$.

3. Results and discussion

VCs can be sought in the form $\psi = \phi(\xi,\eta){\rm e}^{{\rm i}b\zeta}$, where $\phi(\xi,\eta)$ is the stationary solution, b is the propagation constant, and ζ is the rescaled propagation distance. In the numerical calculation, the trial solution is selected as the Laguerre–Gaussian beam

$$\phi = A\left(\frac{\sqrt{2}\rho}{r_0}\right)^{|l|}\exp\left(-\frac{\rho^2}{r_0^2}\right){\rm L}_{\rm p}^{|l|}\left(\frac{2\rho^2}{r_0^2}\right){\rm e}^{{\rm i}l\varphi}, \quad (6)$$

where A is the amplitude, r_0 is the initial width of input beam, and $\rho=\sqrt{\xi^2+\eta^2}$; ${\rm L}_{\rm p}^{|l|}$ is the generalized Lagueree–Gaussian polynomial with l and p, respectively, the radial and azimuthal indices; φ is the azimuthal angle. In the vortex solutions, the radial index l is related the topological charge or vorticity.

Numerical solutions of VCs with various radical index l are obtained by the modified square operator method.[45] We employ the Fourier integral method to solve for the evolution of optical VCs along their propagation direction. The fidelity[43] is adopted to evaluate the stabilities of VCs during

propagation as

$$J=\frac{\left|\int|\psi(\boldsymbol{r},\zeta)\psi(\boldsymbol{r},\zeta=0)|\,\mathrm{d}\boldsymbol{r}\right|^2}{\int|\psi(\boldsymbol{r},\zeta)|^2\,\mathrm{d}\boldsymbol{r}\int|\psi(\boldsymbol{r},\zeta=0)|^2\,\mathrm{d}\boldsymbol{r}}. \tag{7}$$

Here $J\to 1$ means a high-fidelity propagation without or with little deformation. Another parameters is the width of VCs R which is defined as

$$R(\xi,\zeta)=\sqrt{\frac{2\int\xi^2|\psi(\boldsymbol{r},\zeta)|^2\,\mathrm{d}\boldsymbol{r}}{U(\zeta)}}, \tag{8}$$

where $U=\int|\psi(\boldsymbol{r},\zeta)|^2\,\mathrm{d}\boldsymbol{r}$ is the power of VCs.

VCs with the radical index l of Laguerre–Gaussian polynomial ranging from 1 to 6 were observed and presented in Fig. 2. Specifically, when $l=1$, 2, the intensity distribution of the VCs exhibits four distinct peaks. On the other hand, for $l>2$, the VCs possess eight distinct peaks. The phase distribution further reveals that the topological charge is 2 for $l=1$ and 2, while it increases to 4 for the range of $l=3$–6. This is different with conventional Kerr nonlinear medias with Bessel optical lattices.[41,42] Further investigations indicate that the cold Rydberg atomic system with $\mathcal{PT}$-symmetric optical Bessel potential cannot support robust VCs with $l>6$.

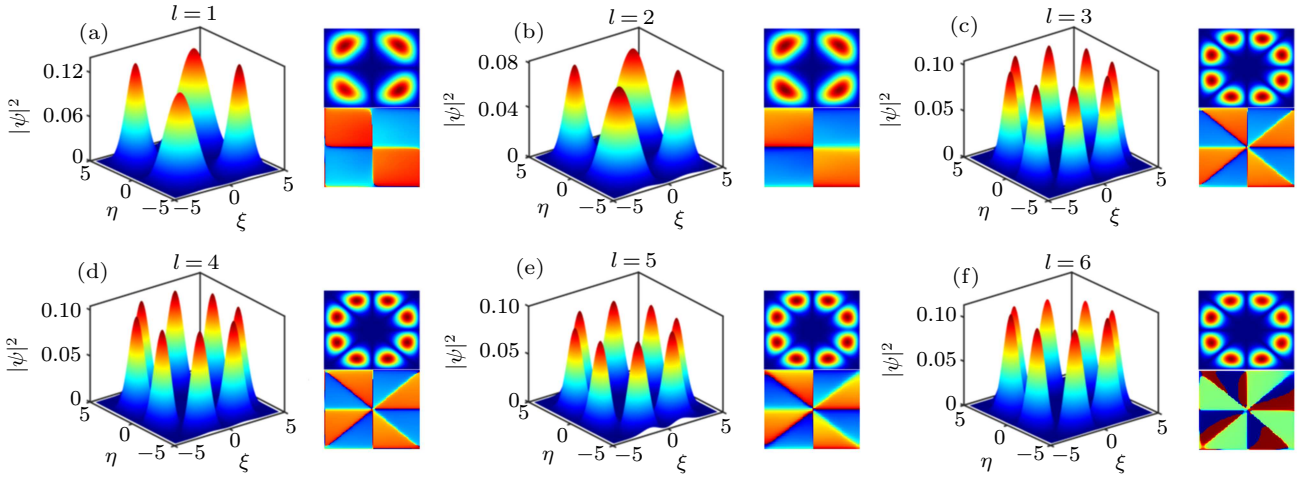


Fig. 2. VCs with radical index $l=1$–6. The profiles, intensity, and phase distribution for each l are displayed in each panel. Four peaks are found with $l=1,2$, and eight peaks are found with $l=3$–6. The parameters are $\sigma=-1$, $\gamma=0.3$, and $(V_0,V_1,V_2)=(2,9,1)$.

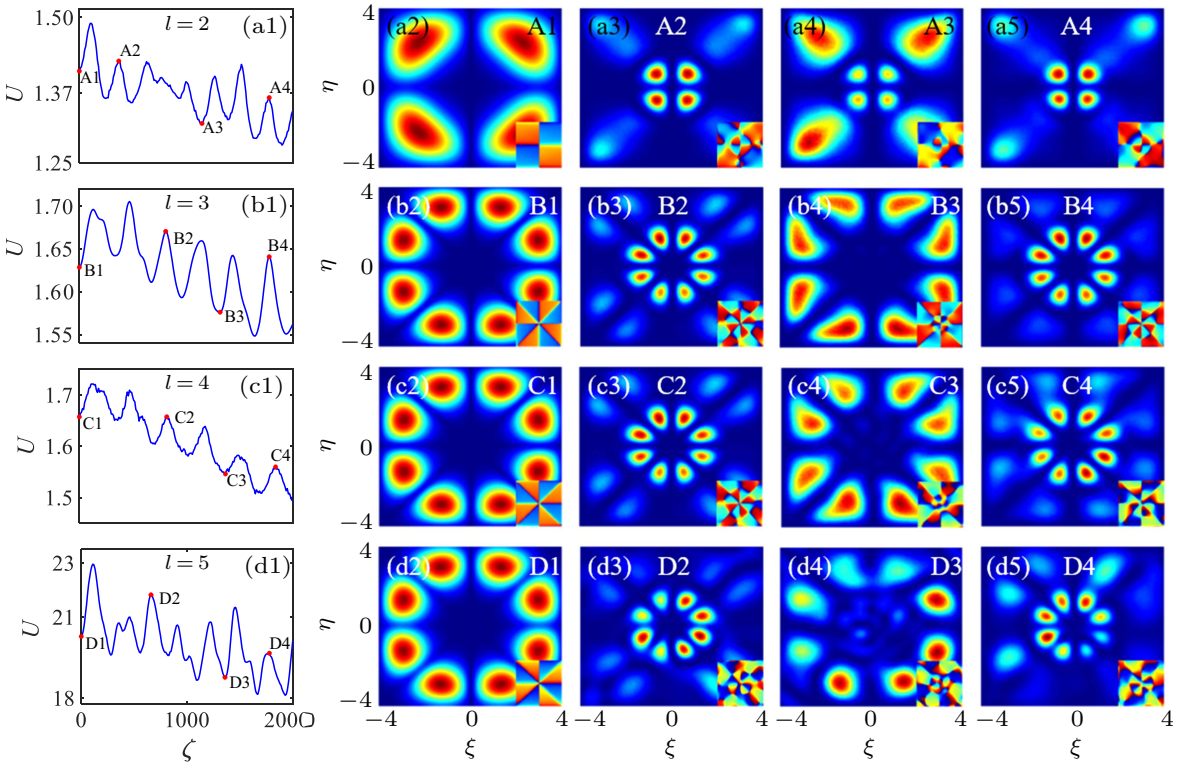


Fig. 3. Evolution of VCs with propagation distance. The first to fourth rows represent the case with $l=2$–5. The first column are power evolution with ζ. The second to fifth columns are profiles of VCs at the points labeled in the first column. The system parameters are the same as Fig. 2.

The propagation dynamics of VCs are presented in Fig. 3, showing the evolution of their profiles and power along the propagation direction. The first to fourth rows correspond to VCs with radical index $l = 2$, 3, 4, and 5, respectively. The first panel in each row illustrates the power during evolution, spanning a propagation distance of up to 1000 units. It is observed that the power of VCs exhibits a quasi-periodic increase and decrease with the propagation distance ζ, manifesting a breathing phenomenon. The profiles of VCs show a synchronous quasi-periodic expansion and extraction. Furthermore, we note a trend of decreasing energy with increasing ζ, indicating energy dissipation during the process of energy exchange between the light fields and optical potential.

To characterize the breathing phenomenon, we define two power states, the inhalation and exhalation phases, respectively, represented by points A2 (A4) and A1 (A3) in Fig. 3(a1). The contour profiles of the VCs at points A1–A4 are displayed in Figs. 3(a2)–3(a5), respectively. For 4-core VCs with $l = 2$, at exhalation phase, the intensity distribution of the VCs is mainly located at outer ring with $(\zeta, \xi) = (0, \pm 3.7)$, corresponding to point A1 in Figs. 3(a1) and 3(a2). This coordinate is the position with the first Bessel lattice well in Fig. 1(c). Conversely, at inhalation phase, the intensity distribution shifts to inner ring at $(\zeta, \xi) = (380, \pm 0.7)$. As the VCs propagate through the medium, their intensity location alternates between these two positions, giving rise to the breathing phenomenon. The breathing period of VCs varies with radical index l. Such breathing phenomenon can also be found in the evolution of 8-core VCs, as shown in Figs. 3(b)–3(d). It is noticed that in the fourth row, the VCs with index $l = 5$ are not robust during the propagation.

During the quasi-periodic oscillation along the propagation distance, the VCs cannot maintain single profile. However, the VCs can keep the breathing behavior for about $\zeta = 1000$. Under parameters given above, this distance ~ 1.2 m in the physical unit which is enough for the experimental observation. This dynamic stability in this work is defined as robust state. The deformation of VCs during propagation in this system is characterized by fidelity J and width R given in Eqs. (7) and (8).

In Fig. 4, it is found that both the J and R exhibit the same quasi-periodic oscillation pattern with the evolution of the power along the propagation distance ζ. Specifically, for various values of $l = 2$, 3, 4, 5, their respective oscillation periods are $\delta\zeta = 250$, 340, 350, and 270, respectively. The second column and the third column present the profiles illustrating the inhalation phase and the exhalation phase of the VCs, with the corresponding states marked as A1 (B1, C1, D1) and A2 (B2, C2, D2) in the first column. Comparing with Figs. 3 and 4, the results reveal that during the inhalation phase and the exhalation phase, the power shift between the inner ring and the outer ring, leading to the synchronized quasi-periodic relation of J and R. Figures 4(d2) and 4(d3) indicate that VCs with $l = 5$ would not keep robust, agreeing with Figs. 3(d2)–3(d5). This breathing behavior may stem from the interaction between the VCs and the propagation medium, resulting in energy exchange between the VCs and the medium. This effect could potentially facilitate the optical signal storage and retrieval in such media.

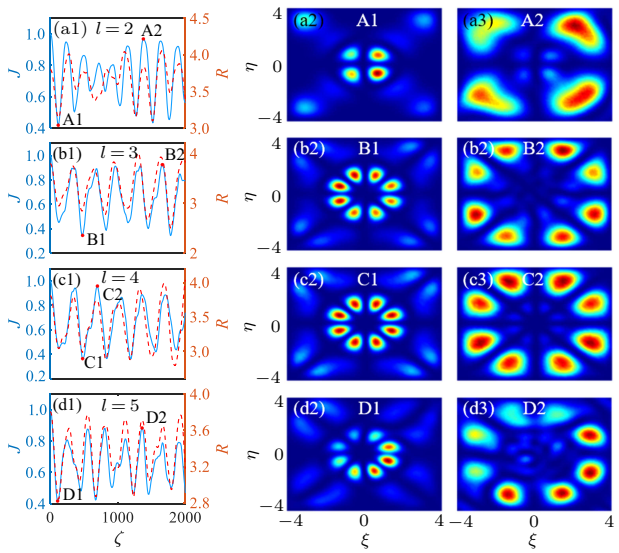


Fig. 4. Fidelity J and width R of VCs during propagation along distance ζ. The radical index $l = 2$, 3, 4, 5 for panels (a), (b), (c), and (d), respectively. The blue solid and red dashed lines represent J and R, respectively. The panels (a2) and (a3) represent the profiles of VCs at points A1 and A2 in panel (a1). The others panels in the second to fourth rows have the same meaning. The system parameters are the same as in Fig. 2.

The periodic fluctuations of the VCs power can be understood by the power current which is defined as $\boldsymbol{S} = \frac{1}{2}(\psi\nabla\psi^* - \psi^*\nabla\psi)$. Here, ψ is the solution of Eq. (3).

Figure 5 illustrates the power current in this system for 4-core and 8-core VCs. As depicted in Figs. 5(a1) and 5(b1), upon completion of the exhalation phase, the primary power current direction is towards the inner ring, while a minor portion flows towards the outer ring. At this stage, the power primarily distributes in the outer ring, and is ready to flow inward. Conversely, after the completion of the inhalation phase, the power current is concentrated within the inner ring, and a minor amount distributed in the outer ring, as shown in Figs. 5(a2) and 5(b2). This phenomenon is consistently observed during the quasi-periodic breathing process of the VCs as they propagate in the ζ direction, as evident in Figs. 5(a3), 5(b3), 5(a4), and 5(b4).

The relationship between the power of VCs and the system parameters, including nonlocal coefficient σ, the propagation constant b, local strength γ, and the imaginary part V_2 of the Bessel lattice potential, is depicted in Fig. 6. The Laguerre polynomials, with radical index l set to 2 and 4, correspond to topological charges of 2 and 4, as inferred from Fig. 2,

represented by blue triangular lines and red square lines, respectively. The dependence of power on Rydberg interactions reveals that robust VCs with 4 cores (blue triangle line) and 8 cores (red square line) are obtained with $\sigma < 0$, as shown in Fig. 6(a). The solid and dashed lines represent the robust and unrubust states of VCs, respectively. As we have known, positive and negative nonlocal nonlinear coefficients represent the self-attractive and self-repulsive interactions in the nonlinear media. For given sets of system parameters in the caption of Fig. 6, the stable domains of the σ corresponding to 4-core and 8-core VCs are $(-1.4$ to $-0.3)$ and $(-1.1$ to $-0.2)$, respectively. This finding indicates that in the context of the present Rydberg-dressed $\mathcal{PT}$-symmetric Bessel lattice potential system, only self-repulsive nonlocal nonlinearities ($\sigma < 0$) can yield robust VCs. Another finding is that the power of 4-core VCs is smaller than 8-core case, indicating a larger stable domain, as shown in Figs. 6(a) and 6(b).

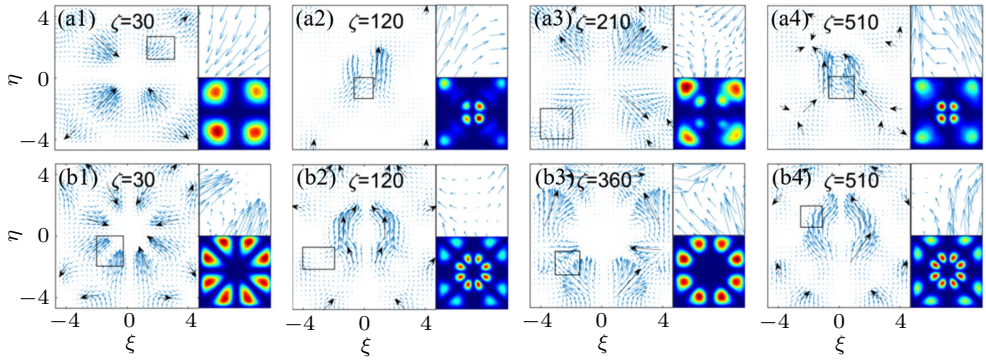


Fig. 5. Power current S with various propagation distances. The radical indices $l = 2$ and 4 for the first and second rows, respectively. The insets in each panel are enlarged power current in the area labeled by square, and the intensity distributions of VCs. The coordinates of intensity distribution is the same with that of power current.

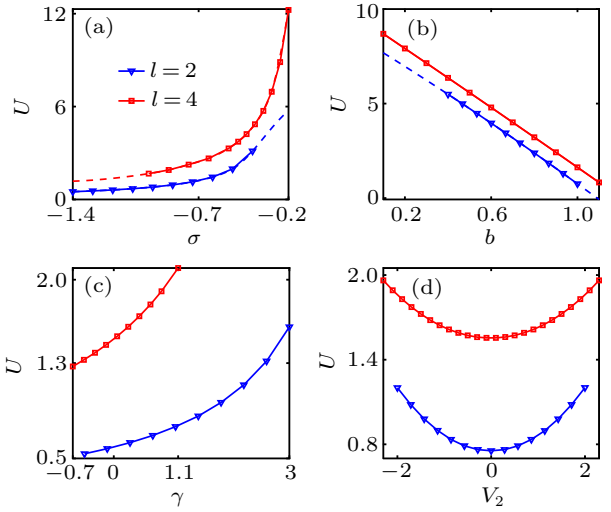


Fig. 6. Dependence of power on nonlocal strength σ (a), propagation constant b (b), local strength γ (c), and imaginary part of Bessel potential V_2 (d). Radical indices $l = 2, 4$ are taken as example, corresponding to 4-core and 8-core VCs. The solid and dashed lines represent the robust and unrobust states of VCs, respectively. For 4-core VCs, the parameters are $l = 2$, $b = 1$, $\sigma = -1$, $\gamma = 1$, $V_0 = 2$, $V_1 = 6$, and $V_2 = 0.1$. For 8-core VCs, $l = 4$, $b = 1$, $\sigma = -1$, $\gamma = 0.3$, $V_0 = 2$, $V_1 = 9$, and $V_2 = 1$.

In the following discussion, the values of nonlocal coefficient for 4-core and 8-core VCs are taken as $\sigma = -1$. A thorough examination of Fig. 6 reveals that the power exhibits similar trends for 4-core and 8-core VCs with variations, such as b, γ, and V_2. Specifically, it decreases and increases monotonously with b and γ, respectively, as shown in Figs. 6(b) and 6(c). The robust VCs are mainly located in the region $\gamma > 0$, and they can still be achieved with $\gamma < 0$, within a narrow range $(-0.7$ to $0)$, signifying a self-repulsive behavior of the medium which is attributed to the collective modulation of the local and nonlocal nonlinear coefficients.

To assess the modulation effects of $\mathcal{PT}$-symmetric lattice potentials on VCs, we varied the imaginary part V_2 of the Bessel lattice potential while keeping the other parameters, as shown in Fig. 6(d). Our findings reveal that the $U(V_2)$ curves for both VCs exhibit a parabolic-like relationship, with the minimum power located at the position $V_2 = 0$. According to the $\mathcal{PT}$-symmetry-broken relation in Fig. 1(f), when the real part of Bessel potential V_1 is fixed, the power of VCs increases with the imaginary part V_2. When V_2 reaches the critical point indicated by the blue line in Fig. 1(f), the system turns from $\mathcal{PT}$-symmetry phase to $\mathcal{PT}$-broken phase, and the VCs become unrobust.

It is observed that the Rydberg nonlocal coefficient σ and the imaginary part of the Bessel potential V_2 have a profound influence on the stability of VCs. As σ or $|V_2|$ increases, the power of VCs increases rapidly, ultimately leading to the disruption of the balance between the dispersion and nonlocal/local nonlinearity within the medium and, consequently, the collapse of the VCs. Beyond the stability domains in Fig. 6, VCs either fail to propagate stably or cannot be generated at all.

Figure 7 presents two examples of unstable VCs, where for the first row, $\sigma = +0.3$, and for the second row, $V_2 = 3$. Notably, in both cases, although the VCs are initially generated, they are unable to propagate long.

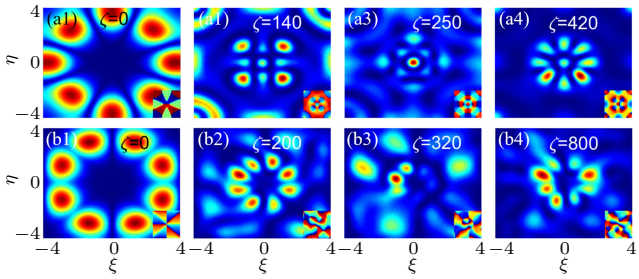


Fig. 7. Examples of unstably propagation of VCs with $l = 4$ by tuning nonlocal strength σ (a) and imaginary part of Bessel potential V_2 (b). In the first and second rows, (σ, V_2) are taken as $(0.3, 1)$ and $(-1, 3)$, respectively. The other parameters are $\gamma = 0.3$, $V_0 = 2$, and $V_1 = 9$.

4. Conclusion

In this study, we investigated a four-level inverted-Y atomic system dressed with Rydberg states. A scheme is proposed to realize an optical Bessel potential with $\mathcal{PT}$-symmetry and explore the possibility of the existence, robust propagation, and active manipulation of vortex clusters in such a $\mathcal{PT}$-symmetric system. Multi-core VCs with four and eight cores, corresponding to topological charges 2 and 4, are obtained by manipulating system parameters, such as the gain-loss component of Bessel lattice potentials, Kerr nonlinearities, and the degree of nonlocality inherent in the Rydberg atoms. Notably, these VCs are mainly confined within the first Bessel lattice well. During propagation, the power and width of VCs undergo a quasi-periodic breathing phenomenon, which is attributed to the power exchange between the light fields and Bessel potential. The profiles keep a synchronous quasi-periodic expansion and extraction with the oscillation of VCs. Both self-attractive and self-repulsive Kerr interactions can sustain robust VCs within this system owing to the combination of local and non-local nonlinearity. By introducing the Bessel potential in the Rydberg atomic system, the topological structure of VCs and their propagation can be well manipulated. This research presented here not only facilitates the creation and manipulation of 2D VCs through $\mathcal{PT}$-symmetric potentials but also paves the way for potential applications in optical information processing and transmission.

Acknowledgements

Project supported by the National Natural Science Foundation of China (Grant No. 62275075), the Science and Technology Research Program of the Education Department of Hubei Province, China (Grant No. B2022188), the Natural Science Foundation of Hubei Province, China (Grant No. 2023AFC042), the Training Program of Innovation and Entrepreneurship for Undergraduates of Hubei Province, China (Grant No. S202210927003), and the Medical Project of Hubei University of Science and Technology (Grant No. 2023YKY08).

References

[1] Kivshar Y S and Agrawal G P 2003 *Optical Solitons: From Fibers to Photonic Crystals* (Cambridge: Academic)
[2] Baizakov B B, Malomed B A and Salerno M 2004 *Phys. Rev. A* **70** 053613
[3] Kartashov Y V, Vysloukh V A and Torner L 2009 *Prog. Opt.* **52** 63
[4] Konotop V V, Yang J and Zezyulin D A 2016 *Rev. Mod. Phys.* **88** 035002
[5] Kartashov Y V, Vysloukh V A and Torner L 2004 *Phys. Rev. Lett.* **93** 093904
[6] Kartashov Y V, Vysloukh V A and Torner L 2005 *Phys. Rev. Lett.* **94** 043902
[7] Kartashov Y V, Carretero-González R, Malomed B A, Vysloukh V A and Torner L 2005 *Opt. Express* **13** 10703
[8] Ruelas A, Lopez-Aguayo S and Gutiérrez-Vega J C 2010 *Phys. Rev. A* **82** 063808
[9] Wang X, Chen Z and Kevrekidis P G 2006 *Phys. Rev. Lett.* **96** 083904
[10] Huang S, Zhang P, Wang X and Chen Z 2010 *Opt. Lett.* **35** 2284
[11] Fleischhauer M, Imamoglu A and Marangos J P 2005 *Rev. Mod. Phys.* **77** 633
[12] Wu Y and Deng L 2004 *Phys. Rev. Lett.* **93** 143904
[13] Huang G, Deng L and Payne M G 2005 *Phys. Rev. E* **72** 016617
[14] Saffman M, Walker T G and Molmer K 2010 *Rev. Mod. Phys.* **82** 2313
[15] Friedler I, Petrosyan D, Fleischhauer M and Kurizki G 2005 *Phys. Rev. A* **72** 043803
[16] Mohapatra A K, Jackson T R and Adams C S 2007 *Phys. Rev. Lett.* **98** 113003
[17] Busche H, Huillery P, Ball S W, Ilieva T, Jones M P A and Adams C S 2017 *Nat. Phys.* **13** 655
[18] Guo Y W, Xu S L, He J R, Deng P, Belić M R and Zhao Y 2020 *Phys. Rev. A* **101** 023806
[19] Yang F, Yang S and You L 2019 *Phys. Rev. Lett.* **123** 063001
[20] Bao S, Zhang H, Zhou J, Zhang L, Zhao J, Xiao L T and Jia S 2016 *Phys. Rev. A* **94** 043822
[21] Jiao Y, Han X, Yang Z, Li J, Raithel G, Zhao J and Jia S 2016 *Phys. Rev. A* **94** 023832
[22] Li B B, Zhao Y, Xu S L, Zhou Q, Fu Q, Ye F, Hua C B, Chen M W, Hu H J, Zhou Q Q and Qiu Z C 2023 *Chin. Phys. Lett.* **40** 044201
[23] Xu S L, Zhou Q, Zhao D, Belić M R and Zhao Y 2020 *Appl. Math. Lett.* **104** 106230
[24] Bai Z, Li W and Huang G 2019 *Optica* **6** 309
[25] Hang C and Huang G 2018 *Phys. Rev. A* **98** 043840
[26] Harris S E 1994 *Opt. Lett.* **19** 2018
[27] Hang C, Konotop V V and Huang G 2009 *Phys. Rev. A* **79** 033826
[28] Bender C M and Boettcher S 1998 *Phys. Rev. Lett.* **80** 5243
[29] Bender C M 2007 *Rep. Prog. Phys.* **70** 947
[30] Hang C, Huang G and Konotop V V 2013 *Phys. Rev. Lett.* **110** 083604
[31] Zhang Z, Zhang Y, Sheng J, Yang L, Miri M, Christodoulides D N, He B, Zhang Y and Xiao M 2016 *Phys. Rev. Lett.* **117** 123601
[32] Xue Y, Hang C, He Y, Bai Z, Jiao Y, Huang G, Zhao J and Jia S 2022 *Phys. Rev. A* **105** 053516
[33] El-Ganainy R, Makris K G, Khajavikhan M, Musslimani Z H, Rotter S and Christodoulides D N 2018 *Nat. Phys.* **14** 11
[34] Suchkov S V, Sukhorukov A A, Huang J, Dmitriev S V, Lee C and Kivshar Y S 2016 *Laser Photon. Rev.* **10** 177
[35] Feng L, El-Ganainy R and Ge L 2017 *Nat. Photon.* **11** 752
[36] Musslimani Z H, Makris K G, El-Ganainy R and Christodoulides D N 2008 *Phys. Rev. Lett.* **100** 030402
[37] Li C, Huang C, Liu H and Dong L 2012 *Opt. Lett.* **37** 4543
[38] Eliezer Y, Bahabad A and Malomed B A 2018 *Phys. Rev. A* **98** 043830
[39] Hu S and Hu W 2012 *J. Phys. B* **45** 225401
[40] Wang H, Wei Y, Huang X, Chen G and Ye H 2018 *Chin. Phys. B* **27** 044203
[41] Chen H and Hu S 2014 *Opt. Commun.* **332** 169
[42] Jin L, Hang C and Huang G 2023 *Phys. Rev. A* **107** 053501
[43] Hang C, Li W and Huang G 2019 *Phys. Rev. A* **100** 043807
[44] Kartashov Y V, Hang C, Huang G and Torner L 2016 *Optica* **3** 1048
[45] Yang J and Lakoba T I 2007 *Stud. Appl. Math.* **118** 153